Joint event location and 3D Poisson's ratio tomography for downhole microseismic monitoring

Congcong Yuan[1], Jie Zhang[1]

[1] *Geophysical Research Institute, School of Earth and Space Sciences, University of Science and Technology of China, Hefei, Anhui 230026, P. R. China*

Congcong Yuan: congcy@mail.ustc.edu.cn

*Jie Zhang (**corresponding author**): jzhang25@ustc.edu.cn*

Running head: Microseismic location and 3D Poisson's ratio tomography

Key words: Seismic tomography; Hydraulic fracturing; Microseismic monitoring.

ABSTRACT

Passive seismic tomography plays a significant role in monitoring subsurface structures and properties during hydraulic fracturing. In this study, we develop a new passive seismic tomography approach to jointly invert for event locations, 3D P-wave velocity (Vp), and Poisson's ratio models, for downhole microseimic monitoring The method enables to directly obtain the 3D Poisson's ratio or Vp/Vs ratio without the assumption of identical P- and S-wave raypaths. We incorporate the back azimuths of passive seismic events into the proposed method to better constrain the event locations. We also apply the 3D cross gradients to the proposed method in order to assimilate the P-wave velocity model with Poisson's ratio model in geological structure. The synthetic experiment demonstrates that the proposed tomographic method is able to recover the event locations and their neighboring 3D P-wave velocity as well as Poisson's ratio models effectively. In the field experiment, microseismic events are relocated reasonably compared with the grid search solutions in a calibrated layer model. The area with low Poisson's ratios may be utilized to estimate the stimulated reservoir volume and indicate a potential area associated with highly saturated hydrocarbon.

Key words: Seismic tomography; Hydraulic fracturing; Microseismic monitoring.

INTRODUCTION

Passive seismic tomography has experienced a long-term developing for obtaining subsurface structures and high-resolution seismc locations (e.g., Chou and Booker 1979; Thurber 1983; Eberhart-Phillips 1990; Hole, 1992; Kissling et al 1994; Zhang and Thurber 2003), since it has been proposed by Crosson (1976) and Aki and Lee (1976). The well-known approach that has been widely applied in the field of seismology helps our understanding of seismotectonic and seismogenic processes over large areas (Thurber *et al.* 1995; Eberhart-Phillips and Michael 1998; Chiarabba and Amato 2003). In regional geothermal or hydrocarbon exploration, passive seismic monitoring has also been successfully applied by Valoroso *et al*. (2008), Simiyu (2009), Zhang *et al.* (2009), and Tselentis *et al.* (2011), because it is relatively economical and environmentally friendly compared to conventional seismic surveys (Durham 2003).

Poisson's ratio or P- and S-wave velocity ratio (Vp/Vs ratio) has the potential to indicate the reservoir lithology and fluid properties (e.g., Tatham 1982; Holbrook *et al.* 1998). It is significant for passive seismic tomography to measure Poisson's ratio or Vp/Vs ratio models instead of Vp or Vs models. The straightforward method is to derive the Poisson's ratio or Vp/Vs ratio by separately inverting Vp and Vs models. The indirect approach has been widely used in the applications for resource prospecting, including (e.g., Barthwal *et al.* 2014; Chatterjee *et al.* 1985; Hauksson and Unruh 2007; Julian *et al.* 1996; Kummerow *et al.* 2012; Lees and Wu 2000; Lees 2002; Zang *et al.* 2014; Yuan and Zhang 2016). The technique is also often employed in the field of seismology, such as (Nakajima *et al.* 2001; Zhao *et al.* 1996; Zhao *et al.* 2010). In the

implementation of the technique, the difference of velcotiy changes in Vp and Vs models leads to the differences of P- and S-wave raypaths. The inconsistence between P- and S-wave raypaths may bring fictitious anomalies into the final Poisson's ratio or Vp/Vs models, thereby misleading the interpretation of reservoir properties (Eberhart-Phillips 1990; Michelini 1993). To address the difficulty deriving from the different ray-coverage and different accuracy of P- and S-wave arrival onsets picking, Michelini (1991) introduced a method to stabilize Vp/Vs model by adding some coupling between Vp and Vs models. Thurber and Atre (1993) assumed the same raypth for P- and S-waves with the residuals of P- and S-wave arrival times. Zhang *et al.* (2009) applied the double-difference tomography (Zhang and Thurber, 2003) to the S-P time differences of the induced seismicity data at a producing petroleum field to estimate the reservoir property. Tselentis *et al.* (2011) presented an alternating seismic tomographic approach for the structural (Vp) and lithological (Poisson's ratio) information, along with the event relocations. Other approaches, such as Walck (1988), Thurber (1993), Koper and Wiens (1999), Lin *el al.* (2007), and Wang (2014), are mainly applied in the field of seismology to characterize the deep structural variations.

To directly delineate the distribution of Poisson's ratio, we propose a new seismic tomograhic method to jointly invert for event locations, 3D Vp, and Poisson's ratio models using the arrival times of P and S waves. Different from the S-P methods (Thurber and Atre 1993; Chiarabba and Amato 2003; Zhang et al. 2009), which assume that the Vp model is perfectly constrained by the P arrivals and that the S paths are identical to the P paths, our proposed method can invert for Vp and Poisson's ratio or

Vp/Vs ratio without the assumption of identical P- and S-wave paths. Additionally, we incorporate back azimuths into the inversion framework to reduce the severity of the non-linearity problem due to the poor ray coverage under single well. We further introduce a 3D cross gradient term into the inversion to constrain Vp and Poisson's ratio or Vp/Vs structures, since the 3D cross gradient is effective to maintain the consistency between two structures in different rock properties (Gallardo and Meju 2003) and may reduce biases in both structural solutions (Tryggvason and Linde 2006). In this study, we first attempt to explicitly introduce the proposed method that jointly inverts for event locations and 3D P-wave velocity as well as Poisson's ratio models. One synthetic experiment is subsequent to demonstrate the validity of the proposed method to accurately recover event locations and 3D P-wave velocity as well as Poisson's ratio. We then apply the proposed method into a field experiment, in which the results are analyzed and interpreted.

THEORY

The proposed method is employed to jointly invert for event locations and 3D Vp as well as Poisson's ratio models using arrival times of P and S waves. In microseismic data processing, the observed arrival time $T_{i,k}$ from a microseismic event i to a receiver k installed in the well is formulated as:

$$T_{i,k} = \tau_i + t_{i,k} \tag{1}$$

$$t_{i,k} = \int_{raypath} \frac{1}{V} dl \tag{2}$$

where $T_{i,k}$ is the observed arrival time. τ_i is the origin time of the event i. $t_{i,k}$ is the traveltime from a microseismic event i to a receiver k. V is the velocity structure. dl is an element of raypath length. The event location, origin time, and velocity structure are the unknowns.

Based on the prior information, the linear approximation of the arrival time residuals can be expressed to the perturbations of the event and velocity model parameters:

$$\Delta T_{i,k} = T_{i,k}^{obs} - T_{i,k}^{cal} = \Delta\tau_i + \sum_{n=1}^{3} \frac{\partial T_{i,k}}{\partial x_n} \Delta x_n + \sum_{l=1}^{raypath} \frac{\partial T_{i,k}}{\partial m_l} \Delta m_l \tag{3}$$

where $T_{i,k}^{obs}$ is the observed arrival time data. $T_{i,k}^{cal}$ represents the calculated arrival time data based on the prior information. $\Delta\tau$ is the origin time perturbation. Δx stands for the event location perturbation. Δm is the perturbation to the slowness ($1/V$). For P-wave, the above equation can be written as:

$$\Delta T_{i,k}^{p} = \Delta\tau_i + \sum_{n=1}^{3} \frac{\partial T_{i,k}^{p}}{\partial x_n} \Delta x_n + \sum_{l=1}^{raypath} \frac{\partial T_{i,k}^{p}}{\partial m_l^{p}} \Delta m_l^{p} \tag{4}$$

For S-wave, the above equation can be written as:

$$\Delta T_{i,k}^{s} = \Delta\tau_i + \sum_{n=1}^{3} \frac{\partial T_{i,k}^{s}}{\partial x_n} \Delta x_n + \sum_{l=1}^{raypath} \frac{\partial T_{i,k}^{s}}{\partial m_l^{s}} \Delta m_l^{s} \tag{5}$$

To directly invert for Vp/Vs and do not to assume identical P and S paths, we convert equation (5) to the following one as:

$$\begin{aligned} \Delta T_{i,k}^{s} &= \Delta\tau_i + \sum_{n=1}^{3} \frac{\partial T_{i,k}^{s}}{\partial x_n} \Delta x_n + \sum_{l=1}^{raypath} \frac{\partial T_{i,k}^{s}}{\partial m_l^{s}} \Delta (m_l^{p} * m_l^{r}) \\ &= \Delta\tau_i + \sum_{n=1}^{3} \frac{\partial T_{i,k}^{s}}{\partial x_n} \Delta x_n + \sum_{l=1}^{raypath} \frac{\partial T_{i,k}^{s}}{\partial m_l^{s}} (\Delta m_l^{p} * m_l^{r} + m_l^{p} * \Delta m_l^{r}) \end{aligned} \tag{6}$$

where m_l^{r} denotes the ratio of V_p and V_s.

Or,

$$\Delta T_{i,k}^{s} = \Delta\tau_i + \sum_{n=1}^{3}\frac{\partial T_{i,k}^{s}}{\partial x_n}\Delta x_n + \sum_{l=1}^{raypath}\frac{\partial T_{i,k}^{s}}{\partial m_l^{s}}(\Delta m_l^{p} * m_l^{r} + m_l^{p} * \Delta m_l^{r})$$

$$= \Delta\tau_i + \sum_{n=1}^{3}\frac{\partial T_{i,k}^{s}}{\partial x_n}\Delta x_n + \sum_{l=1}^{raypath}\frac{\partial T_{i,k}^{s}}{\partial m_l^{s}}(m_l^{r} * \Delta m_l^{p} + \frac{m_l^{p}\left(m_l^{r2}-1\right)^{2}}{m_l^{r}}\Delta m_l^{\upsilon}) \quad (7)$$

where m_l^{υ} denotes the Poisson's ratio.

Before building an inversion scheme for solving the hypocenters, Vp and Poisson's rato simultaneously, we define the objection function for the inversion with respect to these unknown parameters as:

$$\phi\left(X, m^{p}, m^{\upsilon}\right) = \frac{1}{2}\left\| \begin{matrix} T^{p} - J_{p}\left(X, m^{p}\right) \\ T^{s} - J_{s}\left(X, m^{p}, m^{\upsilon}\right) \end{matrix} \right\|^{2} + \frac{1}{2}\left\| \begin{matrix} \tau_{p} L\left(m^{p} - m_0^{p}\right) \\ \tau_{\upsilon} L\left(m^{\upsilon} - m_0^{\upsilon}\right) \end{matrix} \right\|^{2} \quad (8)$$

where J is the sensitivity matrix of the arrival time with respect to the hypocenter (X), P-wave slowness (m^{p}) or Poisson's ratio (m^{υ}). We apply the 3D wavefront raytracing method (Sethian and Popovici 1999) to calculate the synthetic P- and S-wave traveltimes. The details to calculate the sensitivities can be found in Appendice B. Note that in the S-wave raytracing, the utilized S-wave velocity model is converted from the P-wave velocity and Poisson's ratio models. The superscript $\boldsymbol{T}$ denotes transpose. The sensitivities can be found in equation (6) or (7). m^{υ} can be also substituted by m^{r} for the velocity ratio tomography. $\boldsymbol{L}$ is a 3D discrete derivative operator. Here, $\boldsymbol{L}$ plays the role of Tikhonov regularization in the form of the second-order model derivative operators. To remain the structure feature of the initial model (layer model obtained from the sonic logs), we usually apply the Tikhonov regularization operator on $\left(m - m_0\right)$. m_0^{p} and m_0^{υ} are the initial models of P-wave slowness and Poisson's

ratio, respectively. τ is the smoothing factor that controls the model smoothing of degrees. Δm^p and Δm^υ are the perturbations to the P-wave velocity and Poisson's ratio, respectively. ΔX is the perturbation on hypocenter and origin time of events. Because of the poor azimuthal coverage of downhole microseismic monitoring, we incorporate the azimuth into the above equation to constrain the event location. Due to the estimated azimuth φ based on the hodogram analysis (Moriya 2008), we can reduce three unknown parameters $\left(\Delta x_1, \Delta x_2, \Delta x_3\right)$ in ΔX into two unknown parameters $\left(\Delta x_1, \Delta x_3\right)$. Upon one of horizontal location parameters Δx_1 is estimated, the other location parameter Δx_2 can be obtained by the following equation:

$$\Delta x_2 = \tan\left(\varphi\right)\Delta x_1 \tag{9}$$

Assume the geological structure of P- and S-wave velocities is similar, we can apply the 3D cross gradient to constrain the joint inversion. The original idea of the cross-gradient constraint is proposed by Gallardo and Meju (2003, 2004). It has been applied to constrain the structrual similarity of elastic parameters, such as P- and S-wave velocities (Zhu et al. 2015; Manukyan et al. 2018). With the additional term of cross gradient, the equation (8) can be slightly transformed into the following one as:

$$\phi\left(X, m^p, m^\upsilon\right) = \frac{1}{2}\left\| \begin{matrix} T^p - J_p\left(X, m^p\right) \\ T^s - J_s\left(X, m^p, m^\upsilon\right) \end{matrix} \right\|^2 + \frac{1}{2}\left\| \begin{matrix} \tau_p L\left(m^p - m_0^p\right) \\ \tau_\upsilon L\left(m^\upsilon - m_0^\upsilon\right) \end{matrix} \right\|^2 + \frac{1}{2}\left\|\tau_t t\left(m^p, m^\upsilon\right)\right\|^2 \tag{10}$$

where t represents the cross gradient between the Vp and Poisson's ratio models. τ_t denotes the weighting for the cross gradient t. The larger value of τ_t enforces two structures become more similar during the inversion. To avoid explicitly handling the sensitivity matrix associated with hypocenters, 3D Vp and Poisson's ratio models, we

utlize the Gauss-Newton strategy (Aster et al. 2013) to linearize the above objective functions before implementing a conjugate gradient (CG) technique (Scales, 1987) to solve the nonlinear inverse problem in an iterative fashion. The detailed linearization inversion schemes of objective functions (equations 8 and 10) are documented in Appendice A.

SYNTHETIC EXPERIMENT

In this section, we use a synthetic test to validate the effectiveness of the proposed method on the recovery of event locations, 3D P-wave velocity, and Poisson's ratio models. Although the borehole and surface survey geometries are both often applied to monitor the microseismic activities during the hydraulic fracturing, we herein employ the receivers deployed in the borehole for evaluating the proposed method, since the quality of the borehole recordings is higher than that recorded on the surface. We suppose one engineering experiment where one stage of the hydraulic fracturing is performed. An event cloud is assumed to happen during the hydraulic fracturing, meanwhile, the flow paths may be formed since the caused fractures intersect with the existing fractures or faults, thereby the fluids from the intrinsic fractures or pores flow into the hydraulic fractures and production wells and affect the geomechanical properties of the area around the fracturing. Due to the increasing fluid pore pressure, P-wave velocities are decreasing (Christensen 1989) and Poisson's ratios are decreasing (Norton and Maxwell 2013). Because the shale formations are usually formed in the layer structure, we assume the models utilized are layered in the test. We embed one

low Vp anomaly and Poisson's ratio anomaly into the layered Vp and Poisson's ratio models, respectively. Figures 1b and 1c are the layered P-wave velocity and Poisson's ratio models that we construct. Along with the anomaly one event cluster is assumed to happen and be recorded by receivers. We design a survey geometry displayed in Figure 1a, in which the event cloud contains 364 events (marked by red dots) with the spacing of 10 m and the fifteen receivers (marked by black triangles) with the spacing of 10 m are distributed in a vertical array and assumed in a downhole. These events and models shown as Figures 1b and 1c are viewed as the true locations and models, respectively. The S-wave velocity model is derived by the relationship between P-wave, S-wave velocities and Poisson's ratio, before applying the 3D wavefront raytracing to calculate the traveltime data that reached at receivers from the true event locations in the true models. We view the synthetic data as the observed or picked arrival time data in the field situation.

Before initiating the proposed method, we have to set up the initial event locations and P-wave as well as Poisson's ratio models for the optimization. We perturb the X and Z components of true locations by 80 m and 30 m on these events. The perturbation of Y component of event locations is derived from the location perturbation along X direction and the true azimuths that are obtained by the true X and Y components of the true event locations, where the azimuths are assumed to be obtained from the true event locations. The perturbed events are marked by green dots in Figure 2a. The initial Vp and Poisson's ratio models are obtained by perturbing the true layered Vp and Poisson's ratio models without the embedded anomalies. We show these initial models in Figures

1d and 1e. After setting up the initial event locations and models, we apply the proposed method to update these location and model parameters until the convergence and stability of misfit curves of P- and S-wave arrival times in the inversion. The misfit is the Root-mean-squared error calculated between the observed and modeled arrival time data. We exhibit the misfit curves of this inversion in Figure 2, where we can recognize that both P and S misfit curves converge to near zero over fifteen iterations. The inverted event locations are output and displayed in Figure 3. The green, blue, and red dots respectively indicate the initial, inverted, and true event locations. From various views, we observe that the event location solutions recover the true event locations well except for some events placed in the right end, which is due to the poor raypath coverage for these events farther away from the receivers. Adding more monitoring wells or improving receiver coverage may help to enhance the accuracy of event locations. In order to analyze the location errors clearly and quantitively, we compare the inverted event locations with the true event locations and calculate the location difference of each event. The absolute event errors of three location components are shown in Figure 4. Mean event location errors are approximately 15 m, 5 m, and 20 m along X, Y, and Z directions. The events with large indexes are in closer proximity to receivers and have smaller location errors than those events with small indexes. To clearly observe the recovery of the embedded anomalies, we clip other layers and focus on the layers with the anomalies. We show the clipped true and inverted Vp as well as Poisson's ratio models in Figure 5. By the comparison with the true Vp and Poisson's

ratio models, we observe both anomalies are effectively inverted, especially for areas in which the events locate.

FIELD EXPERIMENT

We also apply the proposed method to a field case in Sichuan basin of China. There are thousands of microseismic events are triggered during one hydraulic fracturing. We preprocess the raw waveforms via fundamental frequency filtering and select 775 events with high quality for this study. Three-components recordings of one example event on twelve receivers are shown in Figure 6. The high quality of the data enables us to pick the first-arrival times precisely. Since the arrivals of S waves may be contaminated by the P-wave codas, we apply a hodogram analysis of the P wave polarization to estimate the azimuth of the event raypath with the windowed P-wave arrivals. In Figure 7, we exihibit the sonic logs (gray lines), a vertical receiver array (reverse triangles), initial Vp and Vs layer models (dashed blue lines) that are constructed based on sonic logs, and the corresponding calibrated layer models (red lines) with one perforation shot, which is shown as a red star in Figure 9. The initial Vp and Vs layer models are converted into 3D Vp and Vs grid models with the grid spacing of 10 m before implementing the proposed tomographic method. Based on both grid models, we calculate the Poisson's ratio model. The initial event locations are achieved by the 3D grid search in the initial Vp and Vs models. Upon the event locations are determined, the initial origin times can be easily estimated. After setting up these configurations, with the proposed approach, we output and obtain the inverted event

locations, 3D Vp and Poisson's ratio models after the misfit curves of P- and S-wave arrival times remain unchanged in the inversion. The misfit curves of P- and S-wave arrival times are shown in Figure 8. After 10 iterations, both misfit curves have approached to zero and almost remained unchanged. We terminate the inversion and output all results by the fifteenth iteration.

Figure 9a shows the 3D distribution of the inverted event locations marked by green dots, which seemingly is consistent in the event distribution to the event locations marked by blue dots that obtained with the grid search in the calibrated Vp and Vs models (see dashed blue lines in Figure 7). The location comparison demonstrates that the proposed method is effective and reasonable to recover these event locations. A more detailed comparison can be observed in other plan views of event locations in Figure 9b-d. In addition, we show different views of Vp and Poisson's ratio inversion results and their corresponding ray density models are shown in Figure 10 and 11. The areas where the high-density rays go through are usually regarded as the areas inverted with high resolution. Referring to the right figures in Figure 10 and 11, we observe that the P-wave velocities and Poisson's ratios are updated clearly in the areas with high-density rays. From various views of Vp model, the areas around the event cloud are updated and decreased in P-wave velocity. Besides, focusing on the area with high-density rays, we clearly observe that the Poisson's ratios in the model are updated. From the geological perspective, the fractured area with filled hydrocarbon corresponds to low P-wave velocity and particularly low Poisson's ratio. The areas with low Poisson's ratio may indicate the existing or concentration of hydrocarbon fluids, especially for

the area with high-density rays. Around the event cloud, we may also estimate the reservoir volume stimulated by fracturing as the area may be characterized by the low Poisson's ratio. We may further indicate whether other areas have a potential reserve on the hydrocarbon fluids that we prospect.

DISCUSSIONS

The synthetic and real experiments demonstrate that the proposed method enables us to estimate the 3D Vp, Poisson's ratio, together with event locations simultaneously. In the synthetic experiment, we design the anomalies similar to "vertical sandwich" velocity model utilized in (Kissling *et al.* 1994; Zhang and Thurber 2003), and assume that the anomaly is caused by the hydraulic fracturing in the realistic practice. The proposed approach is able to effectively recover these anomalies and associated event locations in the experiment. However, the imaging resolution is not enough to resolve the changes in these anomalies, because of the insufficient ray coverage and the inherent limitation of raytracing-based tomography. The ray coverage can be enhanced by adding more events, receivers or more monitoring wells, thereby the areas of interest can be better resolved. In the field experiment, we recognize some anomalies with low Poisson's ratios in the areas with high-density rays. We also observe that the event cluster is associated with the low Poisson's ratio. The low Poisson's ratio anomalies may be interpreted due to changes in the rock properties of the shale when the fractures are triggered during the high-pressure fuild injection. The fracturing treatment may fracture the nearby shale rocks and connect pre-existed pores or fractures, which improves the porosity and permeability and enhances the fluid flow or concentration. Hence, one of geomechanical properties, Poisson's ratio, of shale rocks may be decreased due to these changes. We may adopt these anomalies with the low Poisson's

ratio as an indicator for estimating stimulated reservoir volume or seeking other potential areas with rich hydrocarbon reserves.

Because only one monitoring well is used in the field study, we set up one vertical receiver array in the survey geometry of the synthetic experiment. During the inversion, we can almost recover the event locations well with the help of the event azimuths. However, for those events farther from the receivers, the inversion can not recover them well due to the poor ray coverage. More receiver coverage or monitoring wells are therefore suggested to constrain the location of microseismic events. In the inversion, we also apply the 3D cross gradient constraint on the model structures during the inversion process. However, the inverted solutions are almost not influenced by the constraint, since the small scale of the study area doest not affect the similarity of raypaths of P and S waves largely. For the large-scale tomography, the cross-gradient term may play an important role to maintain the similarity between Vp and Poisson's ratio models structurally.

CONCLUSION

In this study, a passive seismic tomographic method is proposed here to jointly invert for 3D Vp, Poisson's ratio, and event parameters. The proposed method enables us to obtain the 3D Poisson's ratio model without the assumption of the identical of P- and S-wave raypaths. We also add the event azimuth into the method to constrain the event location, and cross-gradient term to constrain the structural similarity of Vp and Poisson's ratio models. The synthetic experiment demonstrates the effectiveness of the

proposed method to recover event locations and those models. We further apply the proposed method into a field experiment. It demonstrates the effectiveness of the proposed method by the comparison between the inverted event locations and those event locations that are obtained by the grid search in calibrated velocity models. In the inverted model, the anomalies with low Poisson's ratio may be regarded as the proxy for estimating the stimulated and potential reservoir volumes.

ACKNOWLEDGMENTS

We gratefully acknowledge the financial support of National Key R&D Program of China (Grant No. 2018YFC1504003). We acknowledge the support from GeoTomo, who offered the software package MiVu™ for this study. **Data Availability Statement:** the data that have been used is confidential. **Author contributions:** C. Y. initiated the method and performed the studies, and J. Z. analyzed the method and results, and helped write the manuscript.

REFERENCES

Aki, K. and Lee, W. H. K. 1976. Determination of three-dimensional velocity anomalies under a seismic array using first P arrival times from local earthquakes: 1. A homogeneous initial model. *Journal of Geophysical research* **81**(23), pp.4381-4399.

Barthwal, H. and van der Baan, M. 2014. Passive seismic tomography using recorded microseismicity. 84th SEG Technical Program Expanded Abstracts: *Society of Exploration Geophysicists* 2357-2362.

Chatterjee, S. N., Pitt, A. M. and Iyer, H. M. 1985. Vp/Vs ratios in the Yellowstone national park region, Wyoming. *Volcanology and Geothermal Research* **26**, (3-4), 213-230.

Chiarabba, C. and Amato, A. 2003. Vp and Vp/Vs images in the Mw 6.0 Colfiorito fault region (central Italy): A contribution to the understanding of seismotectonic and seismogenic processes. *Journal of Geophysical Research B: Solid Earth* 108.

Christensen, N. I. 1989. Pore pressure, seismic velocities, and crustal structure, in Pakiser, L.C., and Mooney, W.D., eds., Geophysical framework of the continental United States. *Geological Society of America Memoir* 783–798.

Chou, C. W. and Booker, J. R. 1979. A Backus—Gilbert approach to inversion of travel-time data for three-dimensional velocity structure. *Geophysical Journal International* **59**(2), pp.325-344.

Crosson, R. S. 1976. Crustal structure modeling of earthquake data: 1. Simultaneous least squares estimation of hypocenter and velocity parameters. *Journal of geophysical research* **81**(17), pp.3036-3046.

Durham, L. S. 2003. Passive seismic. Listen: Is it the next big thing? *AAPG Explorer* **24**(4), 127–131.

Eberhart-Phillips, D. 1990. Three-dimensional P and S velocity structure in the Coalinga region, California. *Journal of Geophysical Research, Solid Earth* **95**(B10), 15343-15363.

Eberhart-Phillips, D. and Michael, A.J. 1998. Seismotectonics of the Loma Prieta, California, region determined from three-dimensional Vp, Vp/Vs, and seismicity. *Journal of Geophysical Research: Solid Earth* **103**(B9), 21099-21120.

Gallardo, L. A. and Meju, M. A. 2003. Characterization of heterogeneous near-surface materials by joint 2D inversion of dc resistivity and seismic data. *Geophysical Research Letters* **30**(13).

Gallardo, L. A. and Meju, M. A. 2004. Joint two-dimensional DC resistivity and seismic travel time inversion with cross-gradients constraints. *Journal of Geophysical Research: Solid Earth* **109**(B3).

Hauksson, E. and Unruh, J. 2007. Regional tectonics of the Coso geothermal area along the intracontinental plate boundary in central eastern California: Three-dimensional Vp and Vp/Vs models, spatial-temporal seismicity patterns, and seismogenic deformation. *Journal of Geophysical Research: Solid Earth* **112**(B6).

Holbrook, W. S., Gajewski, D., Krammer, A. and Prodehl, C. 1988. An interpretation of wide-angle compressional and shear wave data in southwest Germany: Poisson's Ratio and petrological implications. *J. Geophys. Res*. **93**, 12081–12106.

Hole, J.A., 1992. Nonlinear high-resolution three-dimensional seismic travel time tomography. *Journal of Geophysical Research: Solid Earth* **97**(B5), 6553-6562.

Julian, B. R., Ross, A., Foulger, G. R. and Evans, J. R. 1996. Three-dimensional seismic image of a geothermal reservoir: The Geysers, California. *Geophysical Research Letters* **23**(6), 685-688.

Koper, K. D., Wiens, D. A., Dorman, L., Hildebrand, J. and Webb, S. 1999. Constraints on the origin of slab and mantle wedge anomalies in Tonga from the ratio of S to P velocities. *Journal of Geophysical Research: Solid Earth* **104**(B7), 15089-15104.

Kummerow, J., Reshetnikov, A., Hring, M. and Asanuma, H. 2012. Distribution of the VP/VS ratio within the Basel 1 geothermal reservoir from microseismic data. *74th EAGE Conference and Exhibition incorporating* EUROPEC.

Kissling, E., Ellsworth, W.L., Eberhart-Phillips, D. and Kradolfer, U. 1994. Initial reference models in local earthquake tomography. *Journal of Geophysical Research: Solid Earth* **99**(B10), 19635-19646.

Lees, J. M. and Wu, H. 2000. Poisson's ratio and porosity at Coso geothermal area, California. *Journal of volcanology and geothermal research* **95**(1), 157-173.

Lees, J. M. 2002. Three-dimensional anatomy of a geothermal field, Coso, southeast-central California: Geologic Evolution of the Mojave Desert and Southwestern Basin and Range. *Geological Society of America Memoir* **195**, 259-276.

Lin, G., Shearer, P. M., Hauksson, E. and Thurber, C. H. 2007. A three-dimensional crustal seismic velocity model for southern California from a composite event method. *Journal of Geophysical Research: Solid Earth* **112**(B11).

Manukyan, E., Maurer, H. and Nuber, A. 2018. Improvements to elastic full-waveform inversion using cross-gradient constraints. *Geophysics* **83**(2), R105-R115.

Michelini, A. and McEvilly, T. V. 1991. Seismological studies at Parkfield. I. Simultaneous inversion for velocity structure and hypocenters using cubic B-splines parameterization. *Bulletin of the Seismological Society of America* **81**(2), pp.524-552.

Michelini, A., 1993. Testing the reliability of V p/V s anomalies in traveltime tomography. *Geophysical Journal International* **114**(2), pp.405-410.

Moriya, H., 2008. Precise arrival time detection of polarized seismic waves using the spectral matrix. *Geophysical Prospecting* **56**(5), pp.667-676.

Nakajima, J., Matsuzawa, T., Hasegawa, A. and Zhao, D. 2001. Three-dimensional structure of Vp, Vs, and Vp/Vs beneath northeastern Japan: Implications for arc magmatism and fluids. *Journal of Geophysical Research: Solid Earth* **106**(B10), 21843-21857.

Norton, M. and Maxwell, S. 2013. Intergrated analysis predicts sweet spots, E&P.

Scales, J. A. 1987. Tomographic inversion via the conjugate gradient method. *Geophysics* **52**(2), 179-185.

Sethian, J. A. and Popovici, A. M. 1999. 3-D traveltime computation using the fast marching method. *Geophysics* **64**(2), 516–523.

Simiyu, S. M. 2009. Application of micro-seismic methods to geothermal exploration: examples from the Kenya Rift. Short Course IV on Exploration for Geothermal Resources, Organized by UNU-GTP, KenGen and GDC, 27.

Tatham, R. H. 1982. Vp/Vs and lithology. *Geophysics* **47**, 336–344.

Thurber, C. H. 1983. Earthquake locations and three-dimensional crustal structure in the Coyote Lake area, central California. *Journal of Geophysical Research: Solid Earth* **88**(B10), pp.8226-8236.

Thurber, C. H. and Atre, S. R. 1993. Three-dimensional Vp/Vs variations along the Loma Prieta rupture zone. *Bulletin of the Seismological Society of America* **83**(3), 717-736.

Thurber, C. H., Atre, S. R. and Eberhart-Phillips, D. 1995. Three-dimensional Vp and Vp/Vs structure at Loma Prieta, California, from local earthquake tomography. *Geophysical Research Letters* **22**, 3079–3082.

Tryggvason, A. and Linde, N. 2006. Local earthquake (LE) tomography with joint inversion for P‐and S‐wave velocities using structural constraints. *Geophysical Research Letters* **33**(7).

Tselentis, G. A., Martakis, N., Paraskevopulos, P. and Lois, A. 2011. High-resolution passive seismic tomography for 3D velocity, Poisson's ratio ν, and P-wave quality QP in the Delvina hydrocarbon field, southern Albania. *Geophysics* **76**(3), B89-B112.

Valoroso, L., Improta, L., De Gori, P., Di Stefano, R., Chiaraluc, L. and Chiarabba, C. 2008. From 3D to 4D passive seismic tomography — The sub-surface structure

imaging of the Val d Agri region, S. Italy. 70th Annual EAGE Conference & Exhibition, *EAGE, Extended Abstracts*, P028.

Walck, M. C. 1988. Three-dimensional VP/VS variations for the Coso region, California. *Journal of Geophysical Research: Solid Earth* **93**(B3), 2047-2052.

Wang, Z. 2014. Joint inversion of P-wave velocity and Vp-Vs ratio: imaging the deep structure in NE Japan. *Applied Geophysics* **11**(2), 119-127.

Yuan, C. and Zhang, J. 2016. 3D microseismic imaging for identifying shale sweet spot. 86th SEG Technical Program Expanded Abstracts, S*EG* 2689-2693.

Zang, A., Oye, V., Jousset, P., Deichmann, N., Gritto, R., McGarr, A., Majer, E. and Bruhn, D. 2014. Analysis of induced seismicity in geothermal reservoirs–An overview. *Geothermics* **52**, 6-21.

Zhang, H. and Thurber, C. H. 2003. Double-difference tomography: The method and its application to the Hayward fault, California. *Bulletin of the Seismological Society of America* **93**(5), 1875-1889.

Zhang, H., Sarkar, S., Toksöz, M. N., Kuleli, H. S. and Al-Kindy, F. 2009. Passive seismic tomography using induced seismicity at a petroleum field in Oman. *Geophysics* **74**(6), WCB57-WCB69.

Zhao, D., Kanamori, H., Negishi, H. and Wiens, D. 1996. Tomography of the source area of the 1995 Kobe earthquake: evidence for fluids at the hypocenter?. *Science* **274**(5294), pp.1891-1894.

Zhao, M., Qiu, X., Xia, S., Xu, H., Wang, P., Wang, T.K., Lee, C.S. and Xia, K. 2010. Seismic structure in the northeastern South China Sea: S-wave velocity and Vp/Vs

ratios derived from three-component OBS data. *Tectonophysics* **480**(1-4), 183-197.

Zhu, T. and Harris, J. M. 2014. Modeling acoustic wave propagation in heterogeneous attenuating media using decoupled fractional Laplacians. *Geophysics* **79**(3), T105-T116.

Appendice A

In this section, we will explicitly linearize the objective functions as shown in equations (8) and (10) with the Gauss-Newton method. Avoid the complexity of many terms in equation (10), we plan to start from minimizing equation (8). From equation (8), the minimization of the objective function can be expressed as:

$$\min\left\{\phi\left(X,m^{p},m^{\upsilon}\right)\right\}=\min\left\{\frac{1}{2}\left\|\begin{matrix}T^{p}-J_{p}\left(X,m^{p}\right)\\T^{s}-J_{s}\left(X,m^{p},m^{\upsilon}\right)\end{matrix}\right\|^{2}+\frac{1}{2}\left\|\begin{matrix}\tau_{p}L\left(m^{p}-m_{0}^{p}\right)\\\tau_{\upsilon}L\left(m^{\upsilon}-m_{0}^{\upsilon}\right)\end{matrix}\right\|^{2}\right\} \tag{A1}$$

Taking the first derivative of the objective funtion to the unknown parameters, we obtain the gradient of the above equation as:

$$\nabla\phi\left(X,m^{p},m^{\upsilon}\right)=-\begin{bmatrix}J_{p}^{T}\left(T^{p}-J_{p}\left(X,m^{p}\right)\right)\\J_{s}^{T}\left(T^{s}-J_{s}\left(X,m^{p},m^{\upsilon}\right)\right)\end{bmatrix}+\begin{bmatrix}\tau_{p}L_{p}^{T}L\left(m^{p}-m_{0}^{p}\right)\\\tau_{\upsilon}L_{\upsilon}^{T}L\left(m^{\upsilon}-m_{0}^{\upsilon}\right)\end{bmatrix} \tag{A2}$$

$$\begin{aligned}\nabla\phi\left(X,m^{p},m^{\upsilon}\right)=&-\begin{bmatrix}J_{p}\left(X\right)&J_{p}\left(m^{p}\right)&0\\J_{s}\left(X\right)&J_{s}\left(m^{p}\right)&J_{s}\left(m^{\upsilon}\right)\end{bmatrix}^{T}\begin{bmatrix}T^{p}-J_{p}\left(X,m^{p}\right)\\T^{s}-J_{s}\left(X,m^{p},m^{\upsilon}\right)\end{bmatrix}\\&+\begin{bmatrix}\tau_{p}L_{p}&0\\0&\tau_{\upsilon}L_{\upsilon}\end{bmatrix}^{T}\begin{bmatrix}\tau_{p}L_{p}\left(m^{p}-m_{0}^{p}\right)\\\tau_{\upsilon}L_{\upsilon}\left(m^{\upsilon}-m_{0}^{\upsilon}\right)\end{bmatrix}\end{aligned} \tag{A3}$$

where $\nabla\phi$ represents the gradient operator of the objection function. Other terms or parameters refer to the theory section. Δm^{p} and Δm^{υ} are the perturbations to the P-wave slowness and Poisson's ratio, respectively. ΔX is the perturbation on hypocenter and origin time of events. The explicit expressions of hypocenter or structure sensitivities in the matrix J can be found in Appendice B.

In the Gauss-Newton method, we can approximate the Hessian matrix with the equation as:

$$H\left(X,m^{p},m^{\upsilon}\right)\approx\begin{bmatrix}J_{p}\left(X\right) & J_{p}\left(m^{p}\right) & 0\\ J_{s}\left(X\right) & J_{s}\left(m^{p}\right) & J_{s}\left(m^{\upsilon}\right)\end{bmatrix}^{T}\begin{bmatrix}J_{p}\left(X\right) & J_{p}\left(m^{p}\right) & 0\\ J_{s}\left(X\right) & J_{s}\left(m^{p}\right) & J_{s}\left(m^{\upsilon}\right)\end{bmatrix}+\begin{bmatrix}0 & \tau_{p}L_{p} & 0\\ 0 & 0 & \tau_{\upsilon}L_{\upsilon}\end{bmatrix}^{T}\begin{bmatrix}0 & \tau_{p}L_{p} & 0\\ 0 & 0 & \tau_{\upsilon}L_{\upsilon}\end{bmatrix} \tag{A4}$$

As equation 9.29 in (Aster et al. 2013), the Newton's method can be perfomed with the gradient operator and the approximate Hessian matrix. We therefore obtain:

$$H\left(X,m^{p},m^{\upsilon}\right)\Delta\left(X,m^{p},m^{\upsilon}\right)^{T}=-\nabla\phi\left(X,m^{p},m^{\upsilon}\right) \tag{A5}$$

where the Hessian and gradient operators correspond to equations (A3-4), respectively. From equation 10 with the cross gradients, the objection function becomes:

$$\min\left\{\phi\left(X,m^{p},m^{\upsilon}\right)\right\}=\min\left\{\frac{1}{2}\left\|\begin{matrix}T^{p}-J_{p}\left(X,m^{p}\right)\\ T^{s}-J_{s}\left(X,m^{p},m^{\upsilon}\right)\end{matrix}\right\|^{2}+\frac{1}{2}\left\|\begin{matrix}\tau_{p}L\left(m^{p}-m_{0}^{p}\right)\\ \tau_{\upsilon}L\left(m^{\upsilon}-m_{0}^{\upsilon}\right)\end{matrix}\right\|^{2}+\frac{1}{2}\left\|\tau_{t}t\left(m^{p},m^{\upsilon}\right)\right\|^{2}\right\} \tag{A6}$$

Similar to solve equation A1, we obtain the gradient and Hessian operators of equation A5. They are derived as:

$$\nabla\phi\left(X,m^{p},m^{\upsilon}\right)=-\begin{bmatrix}J_{p}^{T}\left(X\right) & J_{p}^{T}\left(m^{p}\right) & 0\\ J_{s}^{T}\left(X\right) & J_{s}^{T}\left(m^{p}\right) & J_{s}^{T}\left(m^{\upsilon}\right)\end{bmatrix}^{T}\begin{bmatrix}\Delta T^{p}\\ \Delta T^{s}\end{bmatrix}+\begin{bmatrix}\tau_{p}L_{p} & 0\\ 0 & \tau_{\upsilon}L_{\upsilon}\end{bmatrix}^{T}\begin{bmatrix}\tau_{p}L_{p}\left(m^{p}-m_{0}^{p}\right)\\ \tau_{\upsilon}L_{\upsilon}\left(m^{\upsilon}-m_{0}^{\upsilon}\right)\end{bmatrix}+\tau_{t}^{2}\begin{bmatrix}B_{p} & B_{\upsilon}\end{bmatrix}^{T}t\left(m^{p},\ m^{\upsilon}\right) \tag{A7}$$

$$H\left(X,m^{p},m^{\upsilon}\right)\approx\begin{bmatrix}J_{p}\left(X\right) & J_{p}\left(m^{p}\right) & 0\\ J_{s}\left(X\right) & J_{s}\left(m^{p}\right) & J_{s}\left(m^{\upsilon}\right)\end{bmatrix}^{T}\begin{bmatrix}J_{p}\left(X\right) & J_{p}\left(m^{p}\right) & 0\\ J_{s}\left(X\right) & J_{s}\left(m^{p}\right) & J_{s}\left(m^{\upsilon}\right)\end{bmatrix}+\begin{bmatrix}0 & \tau_{p}L_{p} & 0\\ 0 & 0 & \tau_{\upsilon}L_{\upsilon}\end{bmatrix}^{T}\begin{bmatrix}0 & \tau_{p}L_{p} & 0\\ 0 & 0 & \tau_{\upsilon}L_{\upsilon}\end{bmatrix}+\tau_{t}^{2}\begin{bmatrix}0 & B_{p} & B_{\upsilon}\end{bmatrix}^{T}\begin{bmatrix}0 & B_{p} & B_{\upsilon}\end{bmatrix} \tag{A8}$$

We can therefore gain the linearization equation of the objection function by substituting the gradient and Hessian operators in equation A5. The equation is shown as,

$$\left(\begin{bmatrix} w_x J_p(X) & J_p(m^p) & 0 \\ w_x J_s(X) & J_s(m^p) & w_\upsilon J_s(m^\upsilon) \end{bmatrix}^T \begin{bmatrix} J_p(X) & J_p(m^p) & 0 \\ J_s(X) & J_s(m^p) & w_\upsilon J_s(m^\upsilon) \end{bmatrix}\right.$$

$$\left. + \begin{bmatrix} 0 & \tau_p L_p & 0 \\ 0 & 0 & \tau_\upsilon L_\upsilon \end{bmatrix}^T \begin{bmatrix} 0 & \tau_p L_p & 0 \\ 0 & 0 & \tau_\upsilon L_\upsilon \end{bmatrix} + \tau_t^2 \begin{bmatrix} 0 & B_p & B_\upsilon \end{bmatrix}^T \begin{bmatrix} 0 & B_p & B_\upsilon \end{bmatrix} \right) \begin{pmatrix} (1/w_x)\Delta X \\ \Delta m^p \\ (1/w_\upsilon)\Delta m^\upsilon \end{pmatrix}$$

$$= -\begin{bmatrix} w_x J_p^T(X) & J_p^T(m^p) & 0 \\ w_x J_s^T(X) & J_s^T(m^p) & w_\upsilon J_s^T(m^\upsilon) \end{bmatrix}^T \begin{bmatrix} \Delta T^p \\ \Delta T^s \end{bmatrix} + \begin{bmatrix} \tau_p L_p & 0 \\ 0 & \tau_\upsilon L_\upsilon \end{bmatrix}^T \begin{bmatrix} \tau_p L_p (m^p - m_0^p) \\ \tau_\upsilon L_\upsilon (m^\upsilon - m_0^\upsilon) \end{bmatrix}$$

$$+ \tau_t^2 \begin{bmatrix} 0 & B_p & B_\upsilon \end{bmatrix}^T \begin{bmatrix} 0 & B_p & B_\upsilon \end{bmatrix} \quad \text{(A9)}$$

where t represents the cross gradient between the P-wave slowness and Poisson's ratio models. The cross gradient is explicitly introduced by Gallardo and Meju (2003). τ_t denotes the weighting for the cross gradient t . B_p and B_υ stand for $\partial t/\partial m^p$ and $\partial t/\partial m^\upsilon$, which are the partial derivatives of the cross gradient with respect to the P-wave slowness and Poisson's ratio parameters, respectively. The partial derivatives can be estimated with a finite-difference operator. Accounting for the different magnitudes of the partial derivatives of hypocenters, P-wave slowness, and Poisson's ratio, we set different weightings, w_x and w_υ, for the disparity. The above equation can be solved iteratively with the CG method. During the inversion, different weightings will be tried to obtain satisfied solutions. The CG method can save computing memories storing matrices in above equations. It only require storing the results of a matrix multiplying a vector or its transpose multiplying a vector.

Appendice B

From equations (4-7), the linear approximations of the arrival time residuals are expressed to the perturbations of the hypocenter and structure parameters, provided

with the prior information:

$$\Delta T_{i,k}^{p} = \Delta \tau_i + \sum_{n=1}^{3} \frac{\partial T_{i,k}^{p}}{\partial x_n} \Delta x_n + \sum_{l=1}^{raypath} \frac{\partial T_{i,k}^{p}}{\partial m_l^{p}} \Delta m_l^{p}, \tag{B1}$$

$$\Delta T_{i,k}^{s} = \Delta \tau_i + \sum_{n=1}^{3} \frac{\partial T_{i,k}^{s}}{\partial x_n} \Delta x_n + \sum_{l=1}^{raypath} \frac{\partial T_{i,k}^{s}}{\partial m_l^{s}} (m_l^{r} * \Delta m_l^{p} + \frac{m_l^{p} \left(m_l^{r\,2} - 1 \right)^2}{m_l^{r}} \Delta m_l^{\upsilon}). \tag{B2}$$

In above expansions, the sensitivities of traveltime T with respect to the hypocenter and structure parameters are:

$$J^{p}\left(X\right) = \left[\frac{\partial T^{p}}{\partial \tau} \quad \frac{\partial T^{p}}{\partial x_1} \quad \frac{\partial T^{p}}{\partial x_2} \quad \frac{\partial T^{p}}{\partial x_3} \right],$$

$$J^{s}\left(X\right) = \left[\frac{\partial T^{s}}{\partial \tau} \quad \frac{\partial T^{s}}{\partial x_1} \quad \frac{\partial T^{s}}{\partial x_2} \quad \frac{\partial T^{s}}{\partial x_3} \right],$$

$$J_{p}\left(m^{p}\right) = \left[\frac{\partial T^{p}}{\partial m_1^{p}} \quad \frac{\partial T^{p}}{\partial m_2^{p}} \quad \cdots \quad \frac{\partial T^{p}}{\partial m_N^{p}} \right], \tag{B3-7}$$

$$J_{s}\left(m^{p}\right) = \left[\frac{\partial T^{s}}{\partial m_1^{s}} m_1^{r} \quad \frac{\partial T^{s}}{\partial m_2^{s}} m_2^{r} \quad \cdots \quad \frac{\partial T^{s}}{\partial m_N^{s}} m_N^{r} \right],$$

$$J_{s}\left(m^{\upsilon}\right) = \left[\frac{\partial T^{\upsilon}}{\partial m_1^{\upsilon}} \frac{m_1^{p} \left(m_1^{r\,2} - 1 \right)^2}{m_1^{r}} \quad \frac{\partial T^{\upsilon}}{\partial m_2^{\upsilon}} \frac{m_2^{p} \left(m_2^{r\,2} - 1 \right)^2}{m_2^{r}} \quad \cdots \quad \frac{\partial T^{\upsilon}}{\partial m_N^{\upsilon}} \frac{m_N^{p} \left(m_N^{r\,2} - 1 \right)^2}{m_N^{r}} \right].$$

where,

$$\frac{\partial T^{p}}{\partial \tau} = \frac{\partial T^{s}}{\partial \tau} = 1,$$

$$\frac{\partial T^{p}}{\partial x_n} = -\mathrm{m}^{p} \frac{dx_n}{ds}, \tag{B8-11}$$

$$\frac{\partial T^{p}}{\partial x_n} = -\mathrm{m}^{s} \frac{dx_n}{ds},$$

$$\frac{\partial T^{p}}{\partial m^{p}} = \frac{\partial T^{s}}{\partial m^{s}} = ds.$$

where $x_n \left(\mathrm{n}=1,2,3 \right)$ represents n^{th} component of hypocentral location. ds is the

length of a local ray across a structure cell divided by the entire ray length. As to sensitivity of the hypocentral location, ds in equation B9 denotes the length of a local ray across the starting structure cell and the ray should originate from a hypocenter. dx_n is the projection of ds on the n^{th} direction, which equals to the spatial grid length if the entire space is grided regularly. More details of the hypocenter sensitivity refer to (Thurber, 1996). N is the number of structual cells that a ray acrosses. In the sensitivity matrices, $J\left(m^p\right)$ and $J\left(m^\upsilon\right)$, we only display the sensitivities of the structure cells with one ray. The sensitivities are all zeros for the structure cells without a ray across. In the inversion, the sensitivity matrices are composed from a number of rays, which depends on the hypocenters and receivers, and their row dimension shall keep the same with the size of structural cells.

LIST OF FIGURE CAPTIONS

Figure 1 (a) Survey geometry. (b) The initial P-wave velocity (Vp) model. (c) The initial Poisson's ratio model. (d) The true P-wave velocity (Vp) model. (e) The true Poisson's ratio model.

Figure 2 Root-mean-squared (RMS) misfit curve of the tomography in the synthetic case. The blue dots and red boxes denote the P- and S-wave traveltime misfits, respectively.

Figure 3 The comparison of event locations in different view plans. (a) 3D view; (b) X-Y plan view; (c) X-Z plan view; (d) Y-Z plan view. The red, blue, and green dots are the true, inverted, and initial event locations. The black reverse triangles represent the receivers.

Figure 4 Absolute location errors of three directions between the true and inverted event locations in the synthetic case.

Figure 5 (a, b) The true Vp and Poisson's ratio models with the zoom-in anomaly. (c, d) The tomographic Vp and Poisson's ratio models obtained by the proposed method.

Figure 6 Example three-components recording of one microseismic event from twelve-receiver array. The P- and S-wave arrivals display a high signal-to-noise ratio and are easily picked (marked by red and blue windows) on twelve receivers. The onsets of windows denote the first-arrivals of P and S waves. The horizontal components truncated by these windows with 20 time samples are utilized to estimate the back azimuths by the hodogram analysis (Moriya, 2008).

Figure 7 1D velocity profiles for downhole microseismic monitoring. The sonic

logs acquired in the borehole are represented by gray lines. The solid red lines are the initial P- and S-wave velocity models that are utilized for the tomographic inversion. The dashed blue lines are the calibrated P- and S-wave velocity models, which are used for grid search location. The reverse black triangles are the receiver array to monitor the microseismic events.

Figure 8 Root-mean-squared (RMS) misfit curve of the tomography in the real case. The blue dots and red boxes denote the P- and S-wave traveltime misfits respectively.

Figure 9 The comparison of event locations in different view plans. (a) 3D view; (b) X-Y plan view; (c) X-Z plan view; (d) Y-Z plan view. The blue dots are the event locations with the grid search method in the calibrated model. The green dots are the event locations inverted by our proposed method. The black reverse triangles represent the receivers. The black line is the horizontal well and the red star on the line is the perforation for hydraulic fracturing.

Figure 10 The inverted P-wave velocity model (left) and the P-wave raypath density model (right). (a, b) plan view (Y=0 km), (c, d) plan view (Z=3.15 km), (e, f) 3D map view.

Figure 11 The inverted Poisson's ratio model (left) and the S-wave raypath density model (right). (a, b) plan view (Y=0 km), (c, d) plan view (Z=3.15 km), (e, f) 3D map view.

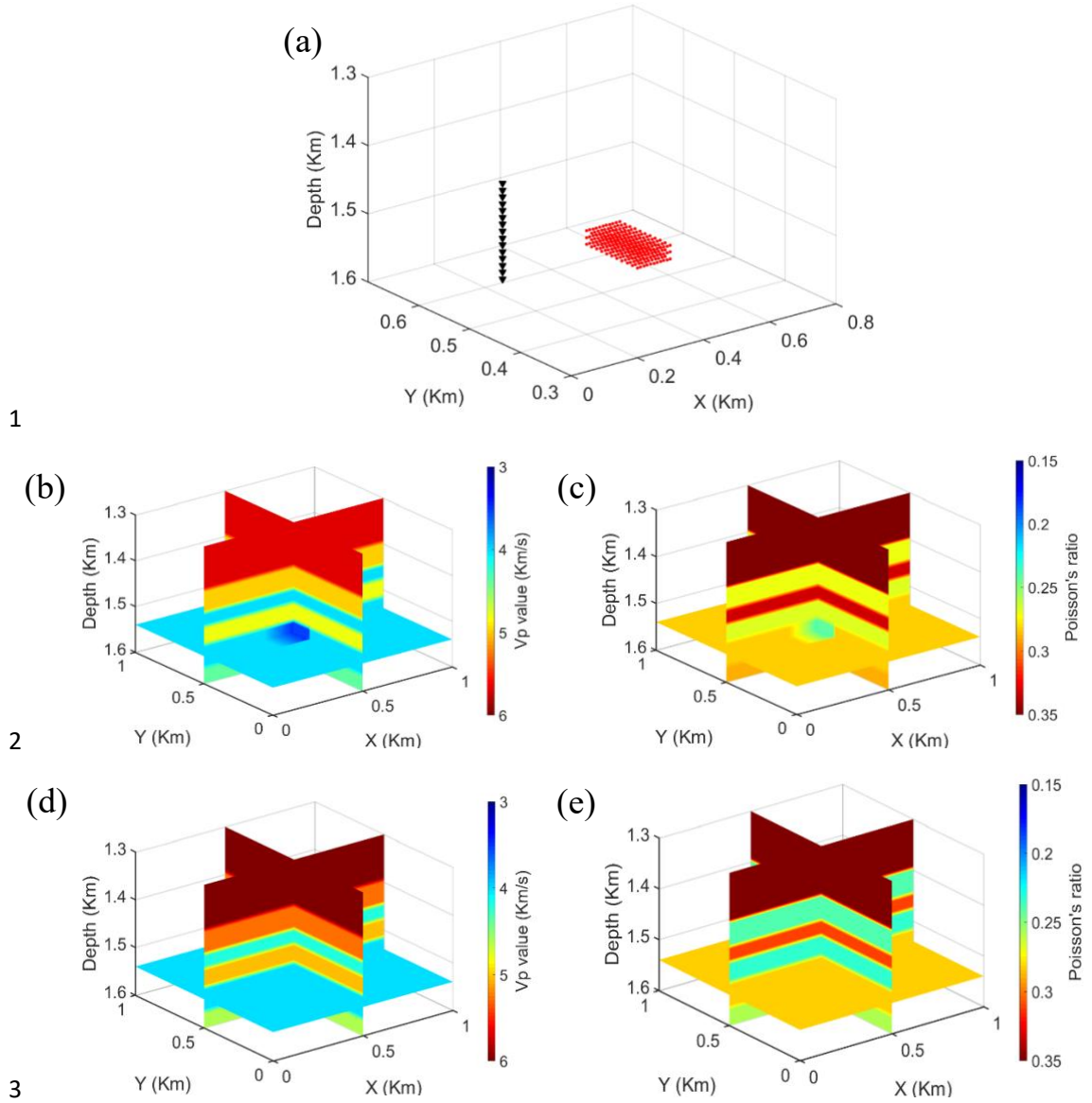

Figure 1 (a) Survey geometry. (b) The initial P-wave velocity (Vp) model. (c) The initial Poisson's ratio model. (d) The true P-wave velocity (Vp) model. (e) The true Poisson's ratio model.

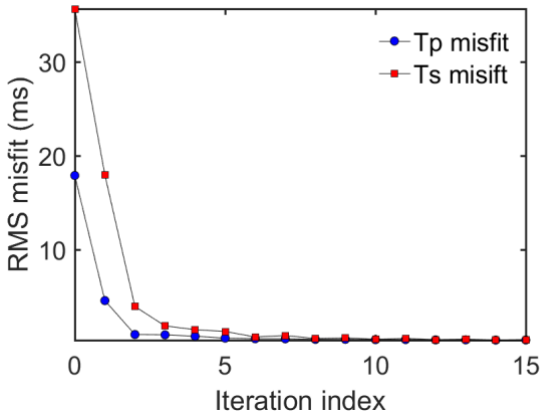

Figure 2 Root-mean-squared (RMS) misfit curve of the tomography in the synthetic case. The blue dots and red boxes denote the P- and S-wave traveltime misfits, respectively.

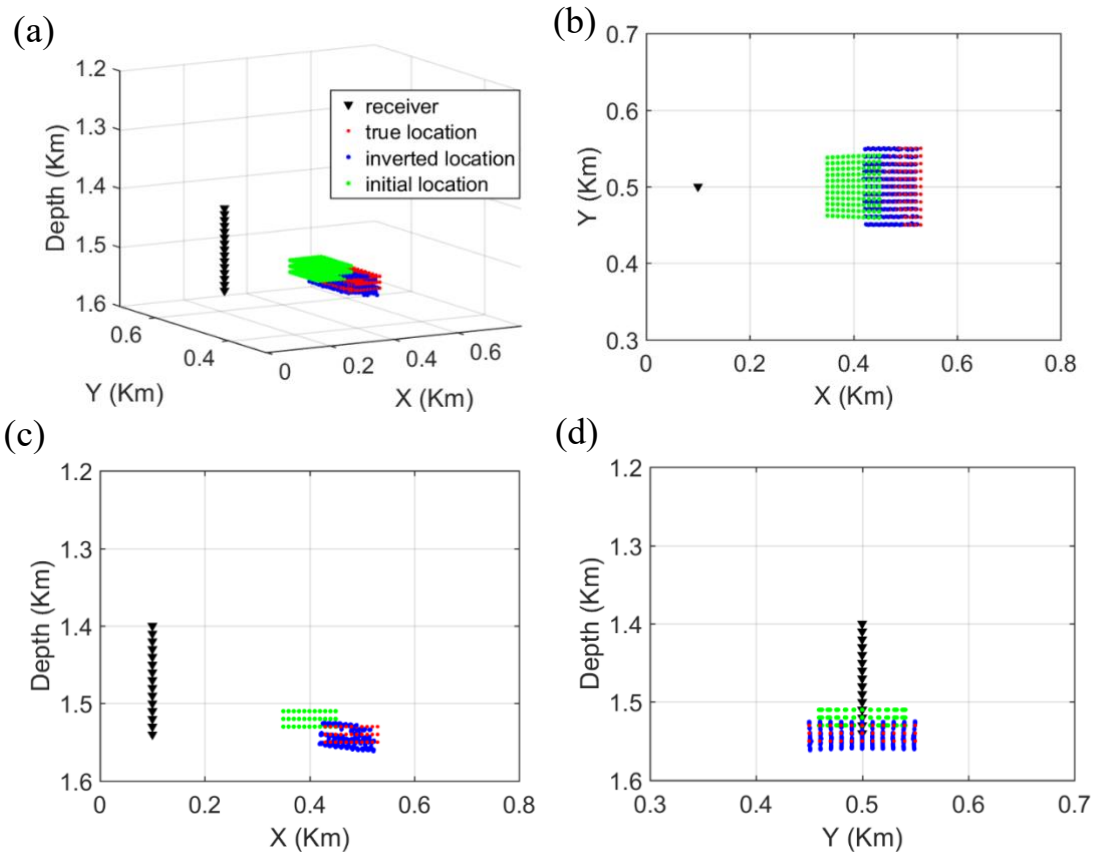

Figure 3 The comparison of event locations in different view plans. (a) 3D view; (b) X-Y plan view; (c) X-Z plan view; (d) Y-Z plan view. The red, blue, and green dots are the true, inverted, and initial event locations. The black reverse triangles represent the receivers.

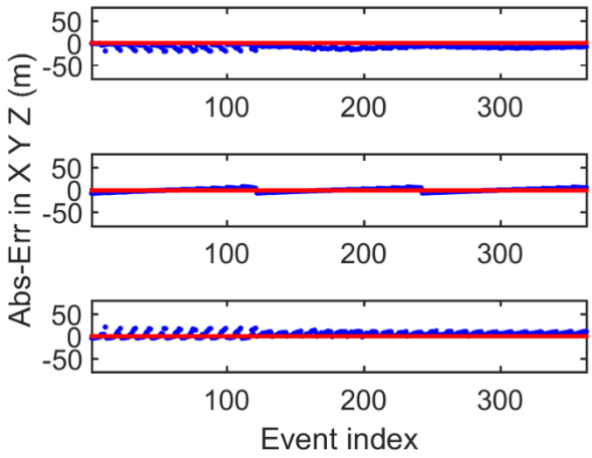

Figure 4 Absolute location errors of three directions between the true and inverted event locations in the synthetic case.

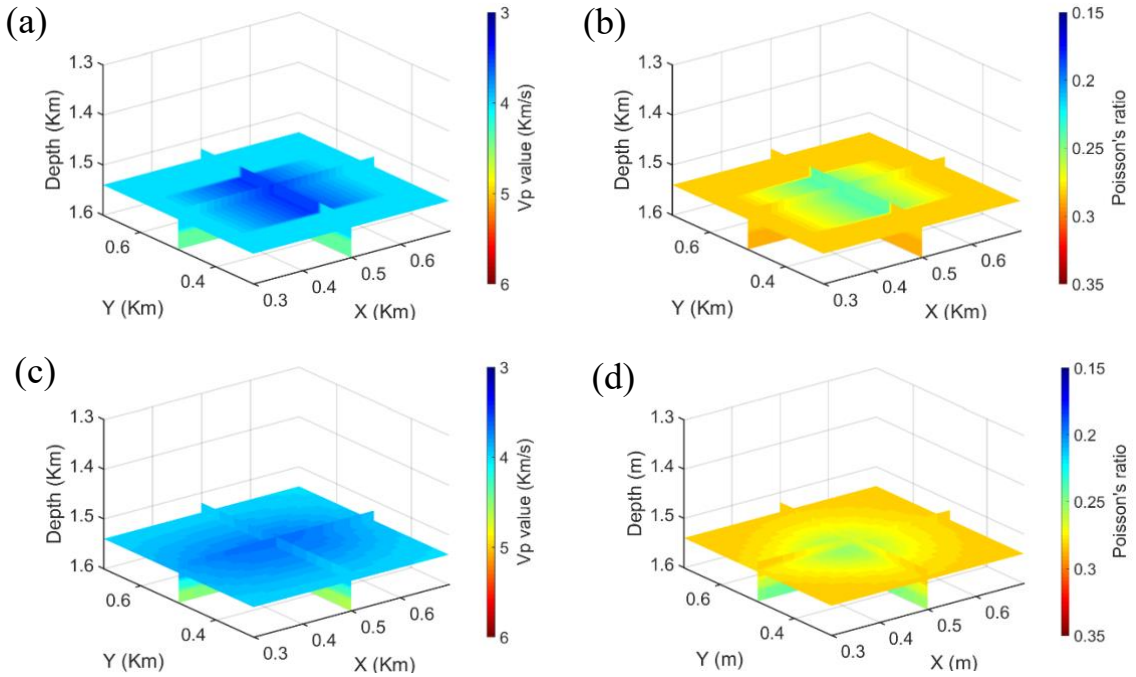

Figure 5 (a, b) The true Vp and Poisson's ratio models with the zoom-in anomaly. (c, d) The tomographic Vp and Poisson's ratio models obtained by the proposed method.

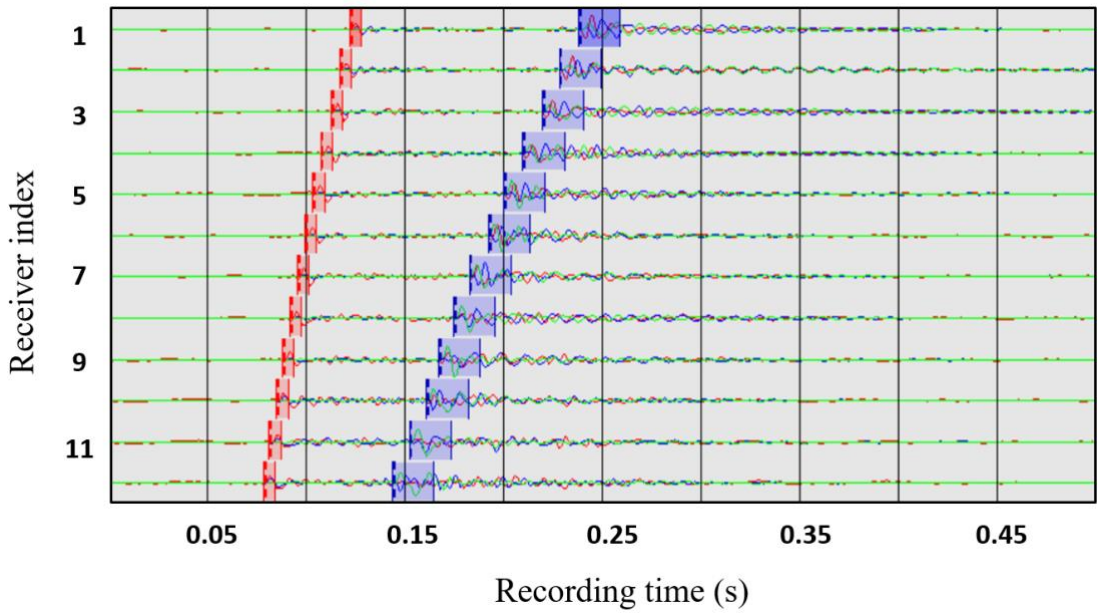

Figure 6 Example three-components recording of one microseismic event from twelve-receiver array. The P- and S-wave arrivals display a high signal-to-noise ratio and are easily picked (marked by red and blue windows) on twelve receivers. The onsets of windows denote the first-arrivals of P and S waves. The horizontal components truncated by these windows with 20 time samples are utilized to estimate the back azimuths by the hodogram analysis (Moriya 2008).

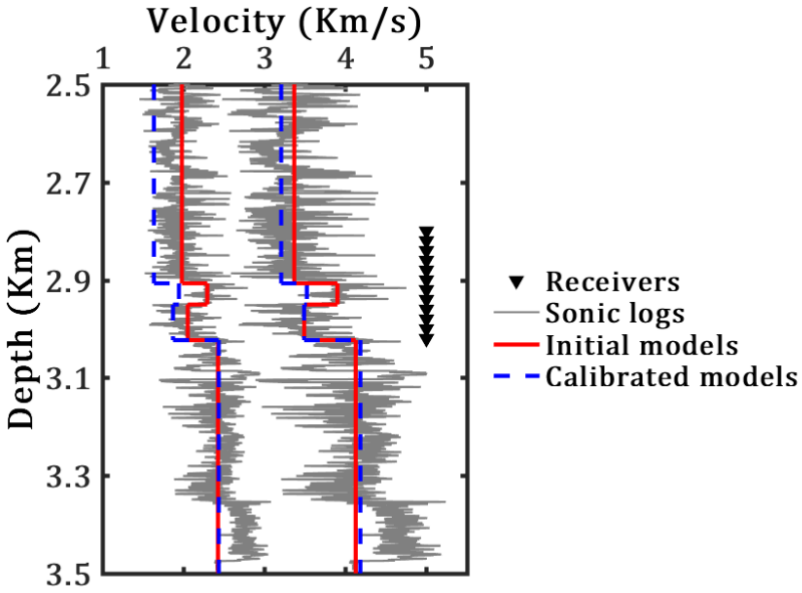

Figure 7 1D velocity profiles for downhole microseismic monitoring. The sonic logs acquired in the borehole are represented by gray lines. The solid red lines are the initial P- and S-wave velocity models that are utilized for the tomographic inversion. The dashed blue lines are the calibrated P- and S-wave velocity models, which are used for grid search location. The reverse black triangles are the receiver array to monitor the microseismic events.

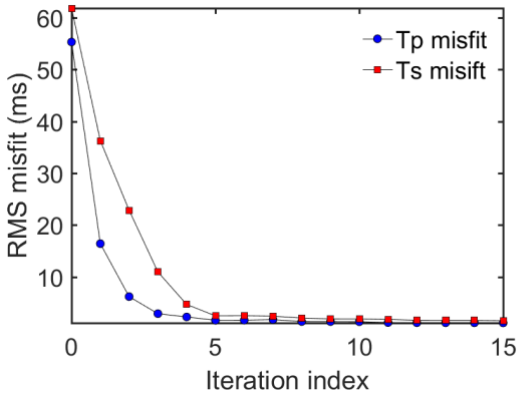

Figure 8 Root-mean-squared (RMS) misfit curve of the tomography in the real case. The blue dots and red boxes denote the P- and S-wave traveltime misfits respectively.

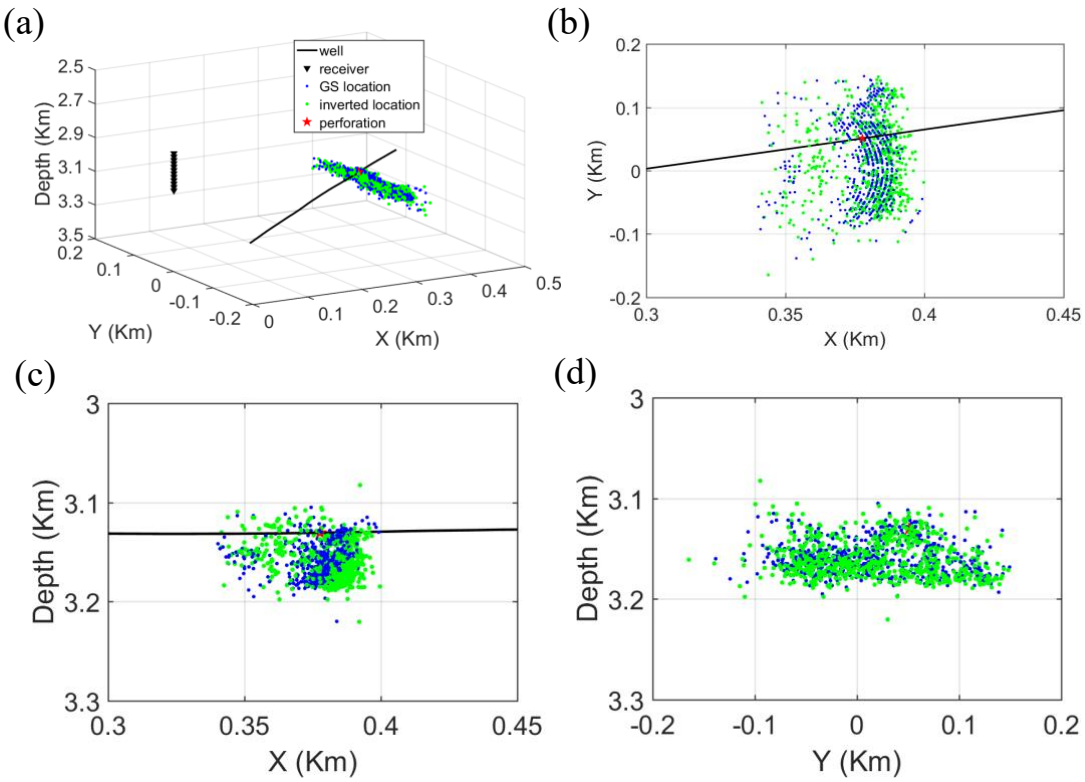

Figure 9 The comparison of event locations in different view plans. (a) 3D view; (b) X-Y plan view; (c) X-Z plan view; (d) Y-Z plan view. The blue dots are the event locations with the grid search method in the calibrated model. The green dots are the event locations inverted by our proposed method. The black reverse triangles represent the receivers. The black line is the horizontal well and the red star on the line is the perforation for hydraulic fracturing.

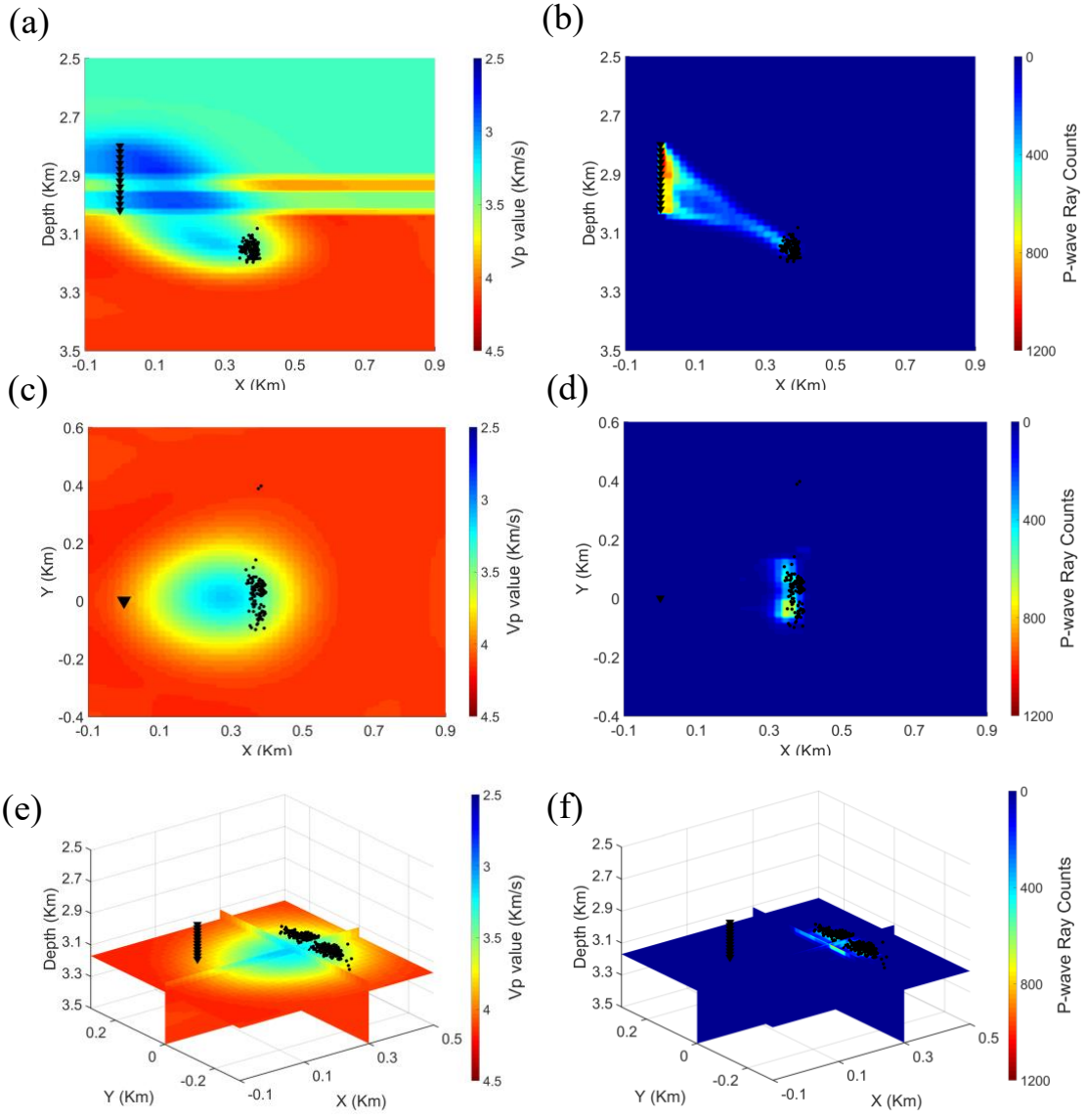

Figure 10 The inverted P-wave velocity model (left) and the P-wave raypath density model (right). (a, b) plan view (Y=0 km), (c, d) plan view (Z=3.15 km), (e, f) 3D map view.

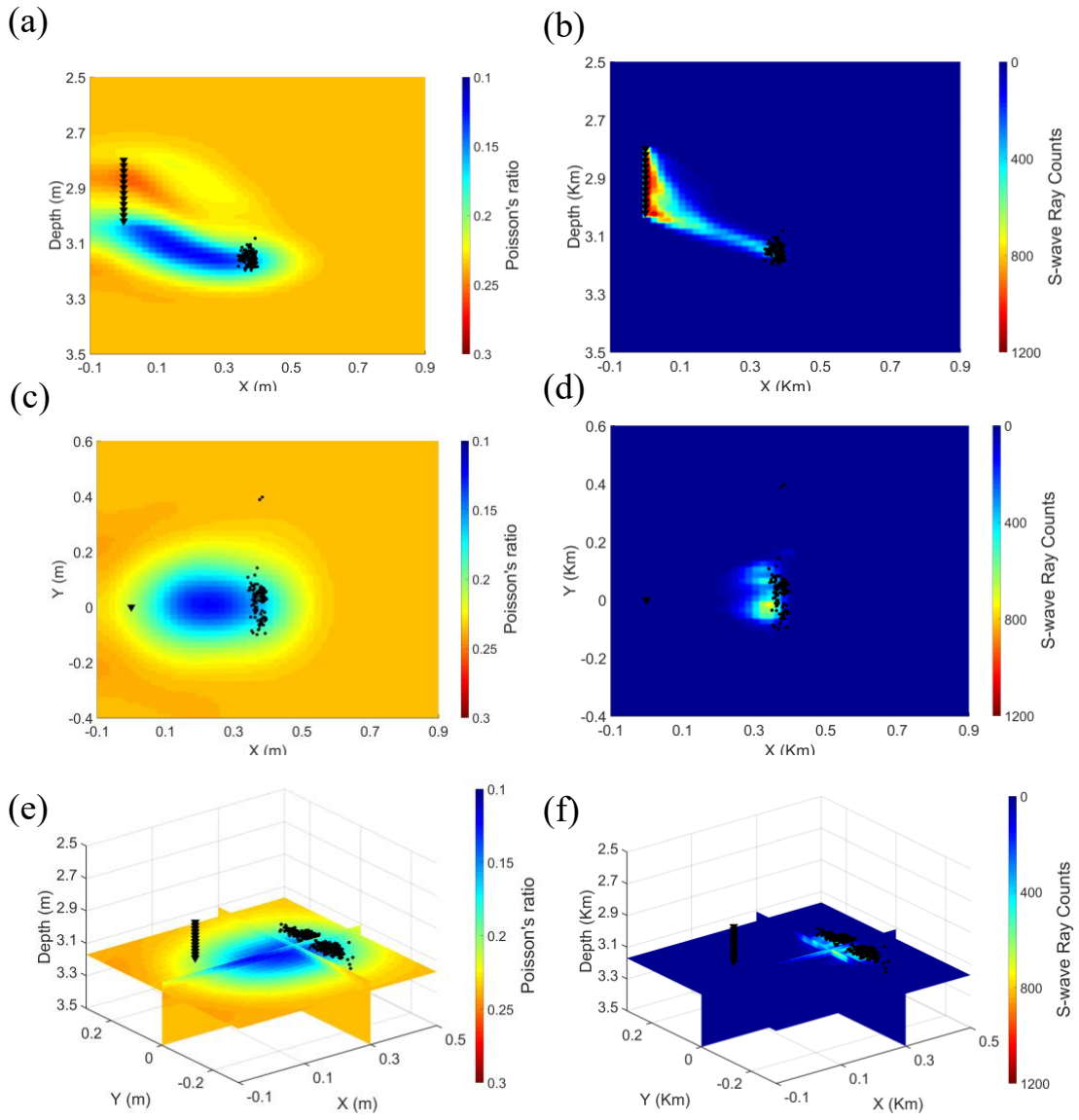

Figure 11 The inverted Poisson's ratio model (left) and the S-wave raypath density model (right). (a, b) plan view (Y=0 km), (c, d) plan view (Z=3.15 km), (e, f) 3D map view.